Published in final edited form as:
Nat Photonics. 2017 October ; 11(10): 639–645. doi:10.1038/s41566-017-0004-4.

In-chip microstructures and photonic devices fabricated by nonlinear laser lithography deep inside silicon

Onur Tokel[#1,‡], **Ahmet Turnali**[#2], **Ghaith Makey**[1], **Parviz Elahi**[1], **Tahir Çolakoğlu**[3], **Emre Ergeçen**[4], **Özgün Yavuz**[2], **René Hübner**[5], **Mona Zolfaghari Borra**[3,6], **Ihor Pavlov**[1], **Alpan Bek**[3,6,7], **Raşit Turan**[3,6,7], **Denizhan Koray Kesim**[2], **Serhat Tozburun**[8,†], **Serim Ilday**[1], and **F. Ömer Ilday**[1,2,9]

[1]Department of Physics, Bilkent University, Ankara, 06800, Turkey

[2]Department of Electrical and Electronics Engineering, Bilkent University, Ankara, 06800, Turkey

[3]The Center for Solar Energy Research and Applications, Middle East Technical University, Ankara, 06800, Turkey

[4]Department of Electrical Engineering and Computer Science, Massachusetts Institute of Technology, Cambridge, Massachusetts, 02139, USA

[5]Helmholtz-Zentrum Dresden - Rossendorf, Institute of Ion Beam Physics and Materials Research, Bautzner Landstraße 400, 01328 Dresden, Germany

[6]Micro and Nanotechnology Graduate Program, Middle East Technical University, Ankara, 06800, Turkey

[7]Department of Physics, Middle East Technical University, Ankara, 06800, Turkey

[8]Harvard Medical School, Boston, MA, 02115, USA

[9]UNAM – National Nanotechnology Research Center and Institute of Materials Science and Nanotechnology, Bilkent University, Ankara, 06800, Turkey

[#] These authors contributed equally to this work.

Abstract

Silicon is an excellent material for microelectronics and integrated photonics1–3 with untapped potential for mid-IR optics4. Despite broad recognition of the importance of the third

[‡]To whom correspondence should be addressed: otokel@bilkent.edu.tr.
[†]Present address: Izmir International Biomedicine and Genome Institute, Izmir, 35340, Turkey

Data availability

The data that support the plots within this paper and other findings of this study are available from the corresponding author upon reasonable request.

Author contributions

A.T. and O.T. contributed equally. O.T. and F.Ö.I designed the research and interpreted the results with help from S.I. Experiments were performed by A.T., O.T., G.M., Ö.Y. The customised laser was built by I.P. Analytical model was developed by P.E., O.T. and F.Ö.I. Numerical simulations were performed by A.T., O.T., E.E. Chemical etching developed by T.Ç, M.Z.B., A.B., R.T. Material analyses were performed by R.H. and S.I. Waveguide characterisation and OCT imaging were performed by D.K.K. and S.T., respectively.

Europe PMC Funders Author Manuscripts

Europe PMC Funders Author Manuscripts

dimension5,6, current lithography methods do not allow fabrication of photonic devices and functional microelements directly inside silicon chips. Even relatively simple curved geometries cannot be realised with techniques like reactive ion etching. Embedded optical elements, like in glass7, electronic devices, and better electronic-photonic integration are lacking8. Here, we demonstrate laser-based fabrication of complex 3D structures deep inside silicon using 1 μm-sized dots and rod-like structures of adjustable length as basic building blocks. The laser-modified Si has a different optical index than unmodified parts, which enables numerous photonic devices. Optionally, these parts are chemically etched to produce desired 3D shapes. We exemplify a plethora of subsurface, *i.e.*, "*in-chip*" microstructures for microfluidic cooling of chips, vias, MEMS, photovoltaic applications and photonic devices that match or surpass the corresponding state-of-the-art device performances.

Efforts to modify silicon below the surface using a pulsed laser go back to more than a decade9, albeit with limited success (see Supplementary Information section 1 for a review). We begin by discussing point-like modification of Si at laser focus, based on an approach we demonstrated10. We use a custom-developed nanosecond-pulsed fibre laser11 operating at a central wavelength of 1.55 μm, where Si is transparent. Using a 40× objective to focus the beam tightly, we trigger a set of light-matter interaction mechanisms simultaneously (Supplementary Information section 2), which leads to well-controlled and repeatable beam collapse (Fig. 1a). When only a single pulse is applied, this results in permanent modification of the crystal structure (Supplementary Information section 3) within a roughly 1 μm-wide spherical region (Fig. 1b). By repositioning the beam and sending a single pulse to each new position, any desired 3D structure, like the 1 μm-thick, 1 mm-long helix in Fig. 1c, can be created, point by point. However, like all 3D fabrication methods, there is an inherent trade-off between resolution, speed and processing volume12. We provide numerous examples of structures and devices in Figures 3 and 4, which occupy volumes ranging between 0.1-10 mm^3. Point-by-point processing such macroscopic volumes with 1-μm resolution requires order of 108–10 beam positioning steps, which corresponds to prohibitively long processing times, limited by the speed of modern beam positioning equipment. We circumvent this problem by augmenting point-by-point processing with creation of self-organized rod-like structures forming along the beam propagation direction. This works well in practice since most 3D structures of interest can be broken down to rods of various lengths (rods grow in length with the number of incident pulses). If the structure indeed requires finer features, these can be created by additional point-by-point processing. This way, the fabrication time is reduced from thousands of hours to mere minutes.

In order to trigger the self-organized pulse-to-pulse growth of the rod-like structures, we invoke nonlinear feedback mechanisms13–16 arising from interaction of infrared laser pulses inside Si: (i) Competing thermal nonlinearity- and free-carrier-induced (FCI) refractive index changes due to counter-propagating laser beams, (ii) a self-limiting, non-local feedback loop arising from permanent local modification of Si at beam focus, which, in turn, iteratively shifts the focal position of the beam, resulting in rod-like structures, whose lengths are controlled by the number of incident pulses. The beam, focussed by a lens, passes through the Si chip; about a third of it returns from the back surface of the chip due to Fresnel reflection and counter-propagates with respect to the incident beam (Fig. 1a). Near

its focal point, positioned at a desired point inside the chip, the beam collapses due to nonlinear effects and modifies Si. When additional pulses are sent, their focal points iteratively shift along the optical (z) axis as each pulse further modifies the material, changing the optical path of the next pulse (Fig. 1a). The beam width is unaltered, so the structured region progressively gets longer without increasing in width, and its aspect ratio can reach far beyond the diffraction limit. By repositioning the beam and sending a controlled number of pulses, we create elongated structures of controllable length (Fig. 2c) at desired locations within the chip, which are combined to construct complex structures (Fig. 1c, 1d). After this single-step procedure, the Si chip has only internal refractive index modification, which is used to demonstrate a variety of optical elements, *e.g.*, lenses, holograms, waveguides. As an optional second step, we can selectively remove the modified regions by chemical etching to enable full 3D sculpting of the entire chip. For instance, the fabrication of Penrose Stairs17 is illustrated in Fig. 2a.

We will explain the self-organisation physics governing the creation of the structures through a toy model (Supplementary Information section 4 for details) to qualitatively illustrate the basic formation mechanism. Wave propagation is governed by the nonlinear paraxial equation and the heat equation. This equation system is mathematically equivalent to the Newton-Schrödinger system18. Two competing diffractive effects dominate beam propagation: Thermally induced change of index of refraction (Δn_{therm}) and free-carrier-induced (FCI) refractive index change (Δn_{FCI}), which are similar to concatenated converging and diverging lenses with focal lengths, f_{therm} and f_{FCI}, respectively. Modification of Si occurs if the beam self-focuses and collapses (the first feedback mechanism), which requires thermal lensing to be stronger than diffraction due to FCI effect ($f_{\text{therm}} < |f_{\text{FCI}}|$). The incident and reflected beams are individually too weak to modify the material ($f_{\text{therm}} > |f_{\text{FCI}}|$), but when overlapped, they cooperate to modify the crystal structure permanently (Fig. 2b). This scenario is verified by numerical solutions of beam propagation based on the split-step Fourier method (Supplementary Information section 2), which show that shielding due to negative Δn_{FCI} precludes subsurface modification for a single beam, consistent with experiments. In contrast, thermal lensing is enhanced when the beams are coupled (Fig. 1a, 2b) and the beam collapses to induce permanent refractive index changes in Si. When more than one pulse is incident, the second feedback mechanism is activated: Each pulse locally modifies silicon; the resulting change in refraction index shifts the focal point for the next pulse similar to the moving focus model of self-focusing19. Focal position of the second pulse, l_2, is given by $\frac{1}{l_2}=\frac{1}{f_{\text{FCI}}}+\frac{1}{f_{\text{therm}}}+\frac{1}{l_1}$, where l_1 is the focal position of the first pulse. The location of the modification caused by the n^{th} pulse (n>1), l_n, is found from $\frac{1}{l_n}=(n-1)\left(\frac{1}{f_{\text{FCI}}}+\frac{1}{f_{\text{therm}}}\right)+\frac{1}{l_1}$. The total length is then $l_{\text{total}}=l_1-l_n=\frac{l_1}{1+\xi/(n-1)}$, where $\xi=\frac{f_{\text{FCI}}f_{\text{therm}}}{l_1(f_{\text{FCI}}+f_{\text{therm}})}$ is a constant. This result reveals that elongation of the structures is self-limiting, stopping before reaching the chip surface (Fig. 2c).

Now, we discuss the features and limitations of creating general 3D structures out of the rod-like building blocks. First, we verify that continuous, wall-like structures can be created by

translating the beam in a plane perpendicular to the beam propagation direction (*z*-axis) (Fig. 1d and Movie S1). Cross-sectional microscope images show that the length of the structures range from the Rayleigh length (~20 μm, Fig. 2c) to ~1 mm (limited by the thickness of the chip), while always retaining a width of ~1 μm (Fig. 1d). The corresponding aspect ratio approaches 1000, which is only possible due to the iterative formation mechanism, whereby previously formed structures are likely to be seeding the process of their elongation. Next, we verify that the structures can cross over each other without distortion, as evidenced by the mesh structure shown in Fig. 1d. We also confirm that curvilinear structures can be formed (see the spiral in Figure S14). None of these features were obvious, *a priori*, due to the self-organised nature of the formation mechanism. There is no fundamental limit to the area over which the structures can be created. Similarly, doping of silicon is not a limitation; we can create them in both intrinsic and doped Si. A complete set of experiments is provided for n- and p-doped Si chips, where the effects of polarisation, scanning angle and direction are analysed (Supplementary Information section 5). Furthermore, we do not observe any asymmetry resulting from the scanning-direction or polarisation of the beam, which is not surprising since Si is a centrosymmetric material20.

We first discuss demonstrations based on purely internal index modification of the Si chip, followed by those where the chip is selectively etched to reveal a desired 3D architecture. There is much interest in using silicon as a material for mid-IR applications4. The capability to locally modify the index of refraction in a well-controlled manner affords unprecedented spatial phase control over optical beams. As an example, we demonstrate the first in-chip Fresnel zone plate (FZP) lens (Fig. 3a). The focal length, f, is determined by $R_k = \sqrt{kf\lambda + (k\lambda/2)^2}$, where R_k is the radius of the k^{th} zone, and λ is the wavelength. An FZP is designed with R_{20} = 1.5 mm, f = 7.2 cm at 1.55 μm. The performance is evaluated to give f = 7.3 cm, M^2 = 1.46 (Fig. 3a) with 15% diffraction efficiency, which exceeds that of single-layer FZP lenses created in glass.

Additional applications of creating a refractive index distribution inside silicon include wavefront structuring 21–23, flat optics24, adaptive optics25, Si photonics1 and better electronic-photonic integration26. We showcase this capability through creation of 2D Fourier computer generated holograms (CGHs) for binary (Fig. 3b) and greyscale (Fig. 3c) images, and Fresnel (Fig. 3d) CGHs for 3D images, all designed using a customised adaptive-additive iterative Fourier transform algorithm (Supplementary Information section 6). The experimentally reconstructed binary hologram, composed of 360 × 360, 10-μm pixels, is shown in Fig. 3b. Reproduction of high-frequency spatial components in holography is notoriously difficult26. The fact that they are reproduced in silicon with high quality is a confirmation of the good control we have over index modifications (Fig. 3b). Greyscale images require even more advanced wavefront structuring, which we demonstrate through a 600 × 600, 10-μm pixel hologram (Fig. 3c). The pixel count and image reconstruction quality of our in-chip holograms are comparable to those of state-of-the-art nanophotonic phase arrays22 and metamaterial phase holograms23,26. We also note that Si is CMOS compatible and lossless over a broad spectral range, including telecommunication wavelengths and much of the mid-IR27. Finally, we demonstrate holography of a 3D image using a Fresnel hologram (800 × 600, 10-μm pixels), which projects rotating rectangles at

consecutive planes (Fig. 3d and Movie S2). This is achieved by first combining a stack of Fourier holograms, each generating a 2D slice of an intended 3D object, and then superimposing them with FZPs, which shift each image to its corresponding focal plane (Supplementary Information section 6). This construction itself is novel, whereby the phase-type Fresnel hologram can be generated without directly using the Fresnel equation. To assess hologram efficiency28, *R*, gratings were written in Si, with

$R=\frac{4F\sin^2(\Delta\phi)}{\pi^2(1-F+F\cos^2(\Delta\phi))}$, where $\Delta\phi$ is the phase modulation and F is the filling factor. The measured first-to-zero order ratio, R ~150% corresponds to $\Delta\phi = 0.69\pi \pm 0.04\pi$, which compares well with the directly measured $\Delta\phi = 0.69\pi \pm 0.01\pi$.

As final applications of purely optical modification of silicon, we demonstrate formation of an optical waveguide (Fig. 3e) and in-chip information storage (Fig. 3f). For the former, we created a 2.5 mm-long tubular waveguide structure since the laser-processed regions have a depressed index of refraction. The radius of the core region is 10 μm. Far-field intensity profile of the beam obtained at the exit of the Si chip is shown in Fig. 3e, where an identical measurement of the beam traversing a region without a waveguide is also provided as control. For the latter, we create multi-level (more than 500 levels are theoretically possible assuming a 1 mm-thick chip; as proof of principle, 25 were written, 7 of which can be directly seen in Movie S3) buried structures arranged in dot or barcode format. Next, we created a two-level barcode, where the levels spell “UFO” and “LAB” (Fig. 3f). We limited ourselves to two levels for ease of readout, which was achieved by optical coherence tomography. Furthermore, laser-written structures could be erased, following exposure to high temperatures (1100 °C) in an oven for 2 hours. Afterwards, the same digital readout protocol that correctly detected 96% of the written dots false-detected only 3% of erased dots (Supplementary Information section 5), highlighting the prospects for erasable and rewritable information storage and holography. This process may likely be simplified and rendered spatially selective by using continuous-wave laser heating instead of an oven.

The second class of applications is based on selective chemical etching of the optically processed chip for truly 3D sculpting (Fig. 4). Thanks to the vastly higher etching rates for modified parts of silicon compared to unmodified parts, we are able to create extremely regular arrays of sharp-edged and high-aspect-ratio (20 μm × 30 μm × 500 μm) pillars within minutes (Fig. 4a and Supplementary Information section 7). Among the numerous possible applications, there is the possibility to create buried microfluidic channels (Fig. 4b). Pumping coolants directly through microfluidic channels written inside chips is being considered as a possible remedy to overheating of microprocessor chips29, which is a main limitation to increasing clock rates30. As a proof-of-principle experiment, we passed cold water through a silicon chip, which decreased the surface temperature by 4 °C within a few seconds (Fig. 4c and Movie S4). As another potential application of 3D sculpting to electronics, we demonstrate through-Si vias31 of controllable depth, including those that cut across the entire chip (Fig. 4d). Further, we show 3D cantilever-like structures that could find use in MEMS applications (Fig. 4e). We also show controlled slicing of a chip into ~30 μm-thick plates (Fig. 4f). To this end, planar sections inside the chip are raster-scanned with laser pulses, followed by chemical etching, resulting in mechanical separation of the chip

Europe PMC Funders Author Manuscripts

along the processed planes. The sliced plates can be used for, *e.g.*, photovoltaic cell fabrication, reducing the required amount of Si material by an order of magnitude with potential for major cost reduction. As a final illustration of the potential for 3D sculpturing, we created a microscale silicon city, *Siliconopolis*, with representations of buildings, trees, a beach and a sea in Fig. 4g.

We have outlined a general methodology and the various examples demonstrated here are far from constituting an exhaustive list. Additional possibilities include the creation of in-chip microlens arrays, microresonators, modulators for multi-level electronic-photonic integration and rewritable holograms or information storage.

Methods

Experimental setup

We used optical pulses with a central wavelength of 1.55 μm, duration of 5 ns and repetition rate of 150 kHz (Supplementary Information section 8). The laser system was coupled to a processing station with precise alignment, power and polarisation control. For single-point modification, a 40× objective with NA of 0.75 was used. For rod-like structures, the laser was focused to ~3 μm (f = 4.5 mm, NA = 0.55) after the back surface of a Si sample, which produced the counter-propagating beam. The samples were translated with a 3-axis high-resolution computer-controlled stage (Aerotech, ANT130-XY, ANT95-L-Z). The pulse energy was controlled by a half-wave plate between two polarising beam splitters (PBS) operating as an attenuator, while the polarisation was linear after the PBS and in the plane of the sample surface. A second half-wave plate was used to control the polarisation angle. Pulse energies were in the range of 2-8 μJ and 15-20 μJ for single-point and rod-like structures, respectively. The modification threshold is estimated to be 5-15 GW/cm^2. Experiments were performed at room temperature and in ambient atmosphere. We anticipate that the multi-beam, multi-pulse based rod-like structures can also be realised in other geometries, such as crossed-laser beams. We used the current architecture for its practical value and simplicity.

Optical coherence tomography and IR microscopy

In order validate the 3D information encoding/decoding capabilities in Si, we used a second-generation optical coherence tomography system called optical frequency-domain imaging (OFDI). The OFDI system uses a polygon filter-based wavelength-swept laser source operating at an axial scan rate of 50 kHz. The sweeping range was over 120 nm at a centre wavelength of 1.3 μm, providing 6-μm axial resolution in air (~1.8 μm in Si). The optical interference signals were digitalised and directly transferred to a hard-drive storage array by a two-channel 100 MS/s data acquisition board (Signatec, Inc.). Approximately 10% of this acquired data was employed and processed on the CPU for real-time structural image feedback. We used a homemade scanner microscope comprising a two-axis galvanometer mirror system (GVS112, Thorlabs, Inc.) and a 10× scan lens (LSM02, Thorlabs, Inc.) for barcode decoding. The barcodes use international symbology UPC, code 128.

A homemade IR microscope was used to evaluate the subsurface structures, which incorporates a broad-spectrum halogen lamp as light source, and an EMCCD camera (Andor, Luca S) as the detector. The IR microscope was operated in the transmission mode with a 20× objective (Nikon, 0.45 NA 20×). Laser-written samples were studied with a reflection mode optical microscope (Nikon, 0.6 NA, 40×) and also with SEM imaging, confirming that no photo-induced modifications on either side of the wafer. In addition, etching results provided additional confirmation of undamaged surfaces after laser writing.

Sample preparation, positioning and scanning

Double-side-polished, <100>-cut, p-type Si samples (boron doped, 1 Ω.cm and 15 kΩ.cm) and n-type (phosphorus doped, 1Ω.cm) were used (Siegert Wafer, GmbH). 500 μm - 1.3 mm thick wafers were diced in 15 mm by 30 mm dimensions. First, a piranha solution was applied to samples (2 minutes). Then, they were cleaned in acetone (5 minutes), ethanol (5 minutes) and deionised water (5 minutes) and finally dried with nitrogen. Si samples were then held in position with neodymium magnets. Precise sample alignment with respect to the laser was found to be crucial. This alignment was accomplished by using interference of multiple reflections from the sample's polished surfaces, which was monitored with an IR sensitive camera. The scheme allowed alignment within a few micrometres throughout the scanning range, and also operated as a proxy for *in-situ* imaging. The scans were performed in a plane perpendicular to the laser propagation direction at speeds in the 0.2-7 mm/s range.

Chemical etching procedure

Chemical etching is applied to optically processed Si samples after the following preparation steps. First, the samples were lapped down 150-250 μm from the surface (Allied High MultiPrep). Consecutive lapping steps were applied with progressively smaller diamond-particle decorated films (with sizes of 35 μm, 9 μm, 6 μm and 0.5 μm). Then, further polishing is performed using an alumina suspension (particle size of 50 nm), until a mirror-like surface is obtained. In order to prevent contamination, the polished surface is cleaned with the Radio Corporation of America (RCA) clean procedure (RCA-1 and RCA-2 steps). The samples were then exposed to the etching solution for a few minutes, in which the molar concentrations of the components, $Cu(NO_3)_2$, HF, HNO_3 and CH_3COOH were 0.05 M, 10 M, 4 M and 3.5 M, respectively (see Supplementary Information section 7). Finally, the samples were rinsed with deionized water and dried with nitrogen flow. All chemicals were supplied by Merck Chemical Company. The average surface roughness of the top surfaces of the etched structures has been measured to be ~20 nm using atomic force microscopy. Although the side surfaces could not be measured directly, we estimate the roughness to be better than ~1 μm. These values are comparable to or smaller than our smallest feature size of 1 μm and the IR wavelengths for which Si is highly transparent (from ~1 μm to ~9 μm).

Supplementary Material

Refer to Web version on PubMed Central for supplementary material.

Acknowledgments

This work was supported partially by the European Research Council (ERC) Consolidator Grant ERC-617521 NLL, EU Marie Curie Fellowship 660769 SMILE, and TÜBITAK under project 113M930. We gratefully acknowledge support by the Structural Characterization Facilities at IBC of the HZDR. We thank H. Volkan Hünerli for discussions on the chemical procedure.

Bibliography

1. Leuthold J, Koos C, Freude W. Nonlinear silicon photonics. Nat Photon. 2010; 4:535–544.
2. Priolo F, Gregorkiewicz T, Galli M, Krauss TF. Silicon nanostructures for photonics and photovoltaics. Nat Nanotech. 2014; 9:19–32.
3. Lim AE-J, et al. Review of silicon photonics foundry efforts. IEEE J Sel Topics Quantum Electron. 2014; 20:405–416.
4. Soref R. Mid-infrared photonics in silicon and germanium. Nat Photon. 2010; 4:495–497.
5. Emma PG, Kursun E. Is 3D chip technology the next growth engine for performance improvement? IBM J Res Dev. 2008; 52:541–552.
6. Wong H-SP, Salahuddin S. Memory leads the way to better computing. Nat Nanotech. 2015; 10:191–194.
7. Beresna M, Gecevičius M, Kazansky PG. Ultrafast laser direct writing and nanostructuring in transparent materials. Adv Opt Photon. 2014; 6:293–339.
8. Sherwood-Droz N, Lipson M. Scalable 3D dense integration of photonics on bulk silicon. Opt Express. 2011; 19:17758–17765. [PubMed: 21935143]
9. Nejadmalayeri AH, Herman PR, Burghoff J, Will M, Nolte S, Tünnermann A. Inscription of optical waveguides in crystalline silicon by mid-infrared femtosecond laser pulses. Opt Lett. 2005; 30:964–966. [PubMed: 15906971]
10. Pavlov, I., Dülgergil, E., Ilbey, E., Ilday, FÖ. Conference on Lasers and Electro-Optics 2012; Optical Society of America; 2012. p. CTu2M.5
11. Pavlov I, Dülgergil E, Ilbey E, Ilday FÖ. Diffraction-limited, 10-W, 5-ns, 100-kHz, all-fiber laser at 1.55 μm. Opt Lett. 2014; 39:2695–2698. [PubMed: 24784080]
12. Truby RL, Lewis JA. Printing soft matter in three dimensions. Nature. 2016; 540:371–378. [PubMed: 27974748]
13. Öktem B, et al. Nonlinear laser lithography for indefinitely large-area nanostructuring with femtosecond pulses. Nat Photon. 2013; 7:897–901.
14. Arecchi FT, Boccaletti S, Ramazza PL. Pattern formation and competition in nonlinear optics. Phys Rep. 1999; 318:1–83.
15. Kerse C, et al. Ablation-cooled material removal with ultrafast bursts of pulses. Nature. 2016; 537:84–88. [PubMed: 27409814]
16. Ilday S, et al. Multiscale self-assembly of silicon quantum dots into an anisotropic three-dimensional random network. Nano Lett. 2016; 16:1942–1948. [PubMed: 26865561]
17. Penrose LS, Penrose R. Impossible objects: a special type of visual illusion. British Journal of Psychology. 1958; 49:31–33. [PubMed: 13536303]
18. Bekenstein R, Schley R, Mutzafi M, Rotschild C, Segev M. Optical simulations of gravitational effects in the Newton-Schrodinger system. Nat Phys. 2015; 11:872–878.
19. Brodeur A, et al. Moving focus in the propagation of ultrashort laser pulses in air. Opt Lett. 1997; 22:304–306. [PubMed: 18183183]
20. Yang W, Kazansky PG, Svirko YP. Non-reciprocal ultrafast laser writing. Nat Photon. 2008; 2:99–104.
21. Kildishev AV, Boltasseva A, Shalaev VM. Planar photonics with metasurfaces. Science. 2013; 339:1232009. [PubMed: 23493714]
22. Sun J, Timurdogan E, Yaacobi A, Hosseini ES, Watts MR. Large-scale nanophotonic phased array. Nature. 2013; 493:195–199. [PubMed: 23302859]
23. Zheng G, et al. Metasurface holograms reaching 80% efficiency. Nat Nanotech. 2015; 10:308–312.

24. Yu N, Capasso F. Flat optics with designer metasurfaces. Nat Mater. 2014; 13:139–150. [PubMed: 24452357]
25. Wang Q, et al. Optically reconfigurable metasurfaces and photonic devices based on phase change materials. Nat Photon. 2016; 10:60–65.
26. Larouche S, Tsai Y-J, Tyler T, Jokerst NM, Smith DR. Infrared metamaterial phase holograms. Nat Mater. 2012; 11:450–454. [PubMed: 22426458]
27. Wu C, et al. Spectrally selective chiral silicon metasurfaces based on infrared Fano resonances. Nat Commun. 2014; 5:3892. [PubMed: 24861488]
28. Li X, et al. Athermally photoreduced graphene oxides for three-dimensional holographic images. Nat Commun. 2015; 6:6984. [PubMed: 25901676]
29. Dang B, Bakir MS, Sekar DC, King CR Jr, Meindl JD. Integrated microfluidic cooling and interconnects for 2D and 3D chips. IEEE Trans Adv Pack. 2010; 33:79–87.
30. Ball P. Feeling the heat. Nature. 2012; 492:174–176. [PubMed: 23235859]
31. Motoyoshi M. Through-silicon via (TSV). Proc IEEE. 2009; 97:43–48.

Europe PMC Funders Author Manuscripts

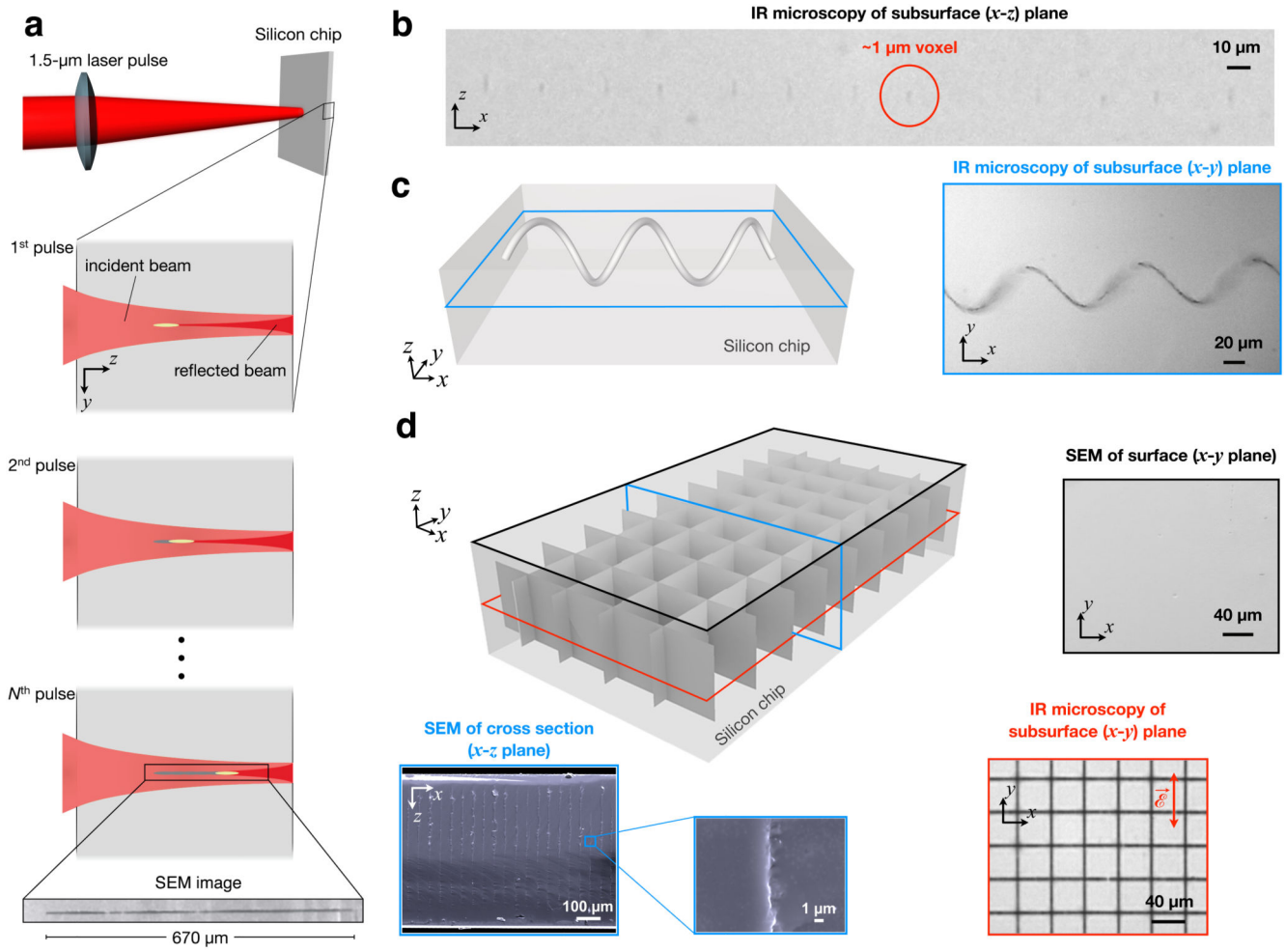

Figure 1. Creation of 3D index modification inside silicon.

(a) The schematic shows laser pulses incident on a Si chip. The pulse collapses and modifies local Si crystal structure, which constitutes a building block for more complex structures. Consecutive laser pulses focus to shifted positions, axially elongating the structured region. The inset shows a scanning electron microscope (SEM) image of a rod-like structure in Si. **(b)** IR image of an array of 1 μm-sized voxels each created by a single laser pulse. **(c)** IR image of a 1 μm-thick, 1 mm-long helix exemplifies point-by-point fabrication of an in-chip 3D structure. **(d)** Various 3D structures can alternatively be formed using rod-like structures as building blocks. These 1-μm wide structures can range from 20 μm to hundreds of micrometres along the laser propagation direction (*z*-axis). SEM (for top surface and cross-section) and infrared (IR) transmission microscope (for subsurface) images correspond to colour-labelled planar sections of the 3D schematic. The subsurface mesh is directly revealed in the IR image, whereas the top (shown) and bottom (not shown) surfaces remain unscathed.

Europe PMC Funders Author Manuscripts

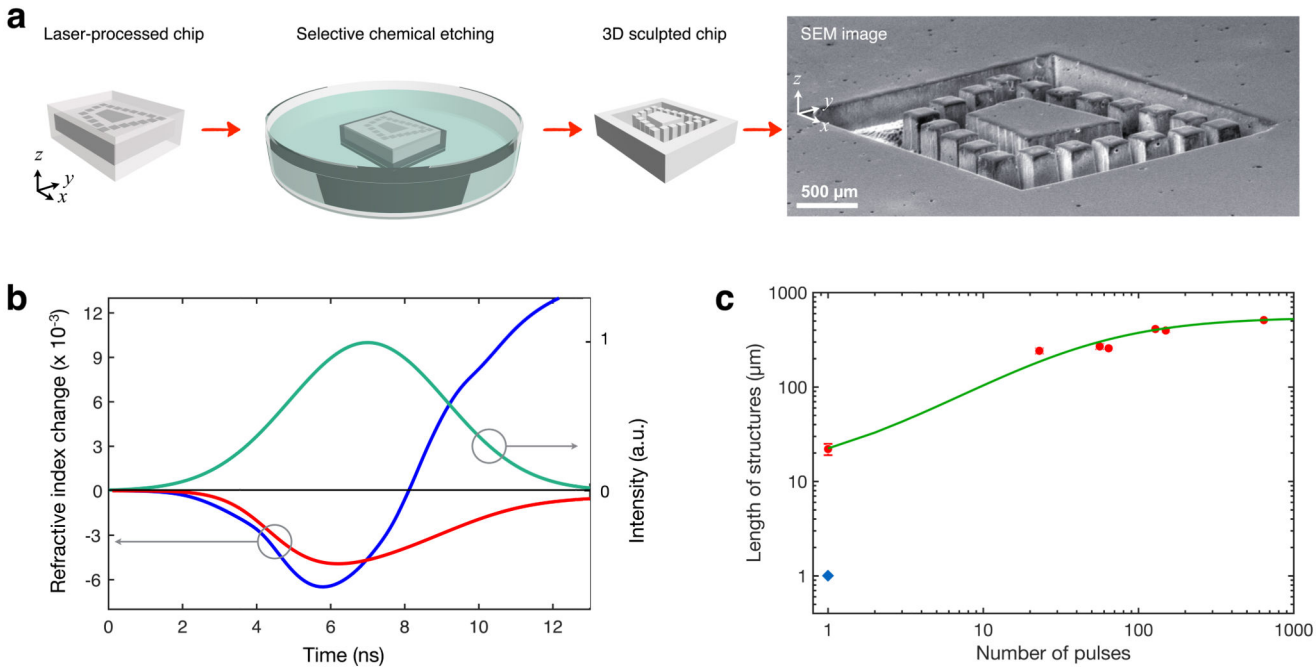

Figure 2. Selective chemical etching and theoretical modelling.

(a) Illustration summarises single-step selective chemical etching for removal of the laser-processed volumes. The SEM image shows experimental realisation of Penrose Stairs16. **(b)** Simulation results show self-induced refractive index change, comprised of thermal nonlinearity (positive $\Delta n_{\text{thermal}}$) and free carrier induced refractive index change (negative Δn_{FCI}) for a single pulse (green curve). The red curve shows the self-induced refractive index change for a single beam focused in Si. The blue curve shows the index change for the two counter-propagating beams. The thermal nonlinearity is dominant in the latter, enabling beam collapse and modification in Si. **(c)** Prediction of our analytic model for structure elongation with each pulse is compared with experiments. Data points represented with red circles were created using a lens with NA of 0.55 and the isolated data point represented by a blue diamond was created using an objective with NA of 0.75. In all figures, *z*-axis is the optical axis.

Europe PMC Funders Author Manuscripts

Europe PMC Funders Author Manuscripts

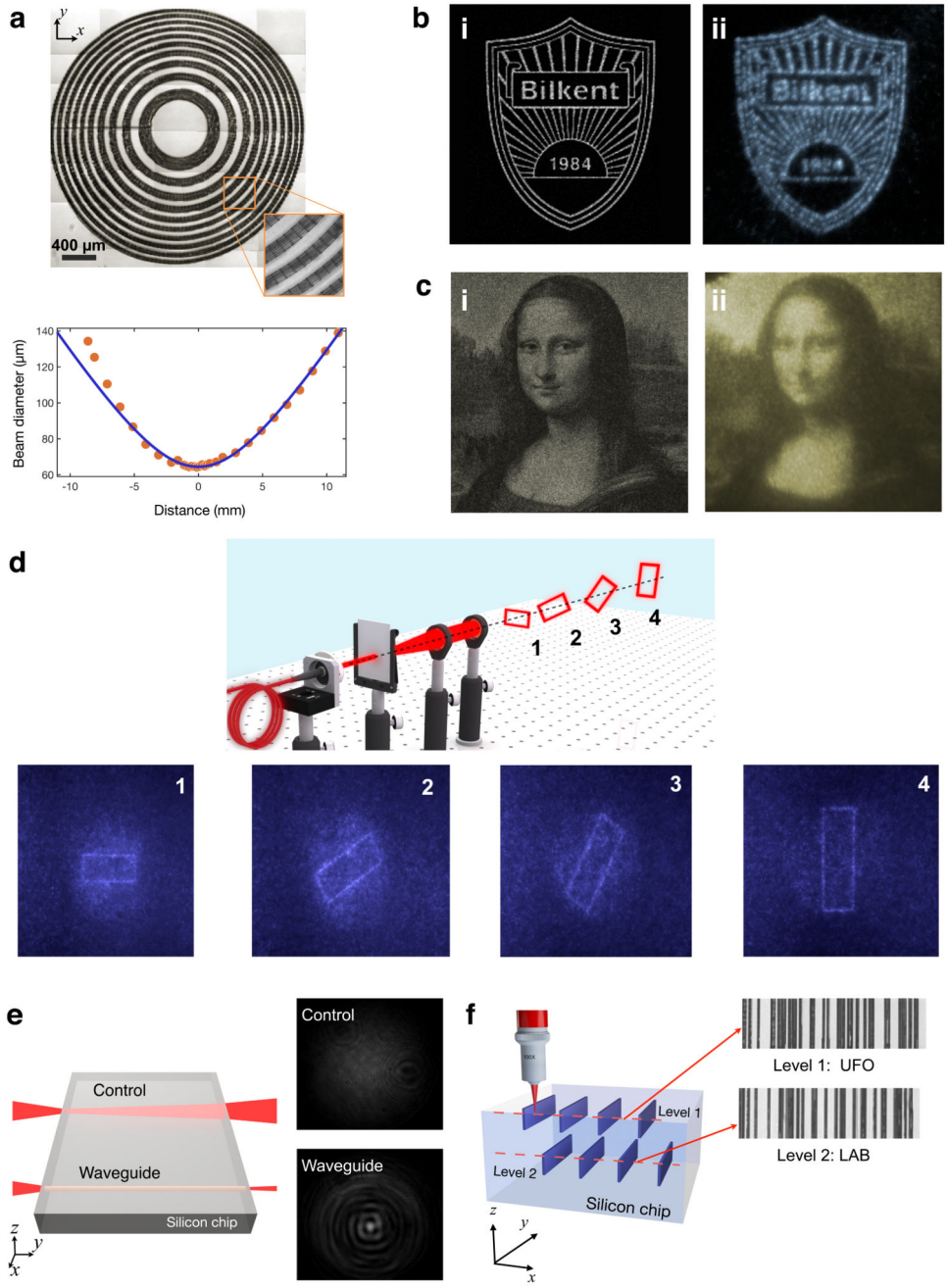

Figure 3. Functional in-chip optical elements and information storage.

(a) Composite IR transmission microscope image of a subsurface Fresnel-zone-plate lens (top). The scale bar is 400 μm. Inset shows a close-up view. Theoretical and experimental beam profiles during focusing are shown (bottom). **(b)** Simulation of a binary image with high spatial components, from a hologram of 356 × 356 pixels **(i)**. Experimental reconstruction of the hologram written in Si **(ii)**. **(c)** Simulation of a grey-scale image of Mona Lisa, from a hologram of 600 × 600 pixels **(i)**. Experimental reconstruction of the hologram written in Si **(ii)**. **(d)** 3D holography of a rotating rectangle at four consecutive

planes (top). The Fresnel-type hologram in Si is comprised of 800 × 600 pixels. Experimentally reconstructed images of the projected rectangles are shown below. All holograms have 10-μm sized square pixels. **(e)** Measured far-field intensity profiles corresponding to the beam traversing a region without a waveguide (control) and a laser-written waveguide. **(f)** Illustration of multi-level information storage and their measured images in Si. Level 1 barcode spells UFO, and Level 2 barcode spells LAB.

Europe PMC Funders Author Manuscripts

Europe PMC Funders Author Manuscripts

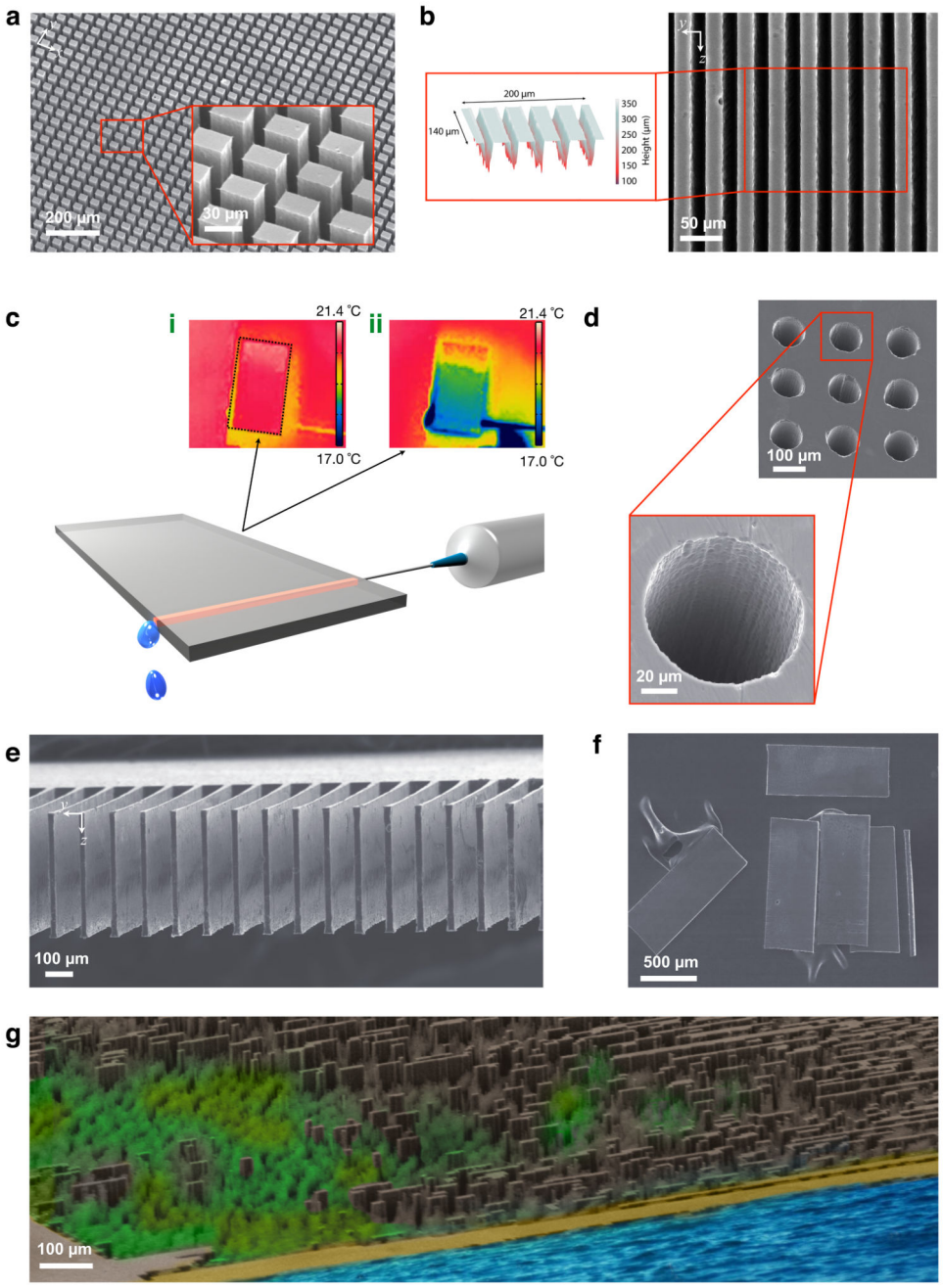

Figure 4. Sculpting of 3D arbitrary micro-architectures.

(a) SEM image of large-area covering, high-aspect-ratio micropillars revealed after chemical etching. The inset shows a close-up view of the etched micropillar array. The pillars have 20 × 30 µm top surfaces, and their heights extend ~500 µm along the laser propagation direction. **(b)** SEM image of a sidewall of a Si chip, showing embedded microchannels. Inset shows laser scanning microscopy of the channels, which penetrate hundreds of micrometres into the chip. **(c)** The illustration shows an 8 mm-long microfluidic channel carrying cooling water into a chip. Thermal camera images **(i)** before and **(ii)** after passing the water shows

that the surface temperature of the chip decreases by 4°C within a few seconds. **(d)** SEM image of entrance of through-Si vias that cut across the entire chip. **(e)** SEM image of 3D cantilever-like structures. **(f)** SEM image of controlled slicing of a chip into ~30 μm-thick plates. **(g)** An artificially coloured view of a micro-cityscape created out of silicon.

Europe PMC Funders Author Manuscripts